processes

MDPI

Article

Efficient Adsorption of Tl(I) from Aqueous Solutions Using Al and Fe-Based Water Treatment Residuals

Youze Xu [1], Yingjun Qing [1,2], Ruimin Gu [1], Shuang Zhou [1], Guangyi Fu [1] and Yuanyuan Zhao [1,*]

[1] Key Laboratory of Water Pollution Control Technology, Hunan Research Academy of Environmental Sciences, Changsha 410004, China
[2] Department of Environment, College of Environment and Resources, Xiangtan University, Xiangtan 411105, China
* Correspondence: zyyhjgc0601@163.com

Abstract: Iron and aluminum water treatment residuals from a water supply plant were used as adsorbents for Tl(I) to treat thallium-containing Tl(I) wastewater and realize the resource utilization of water treatment residuals. The feasibility study results showed that Fe-WTR and Al-WTR reached adsorption equilibria within 120 min. The Langmuir model showed maximum adsorption capacities of Tl(I) on Fe-WTR and Al-WTR as 3.751 and 0.690 mg g^{-1} separately at an initial concentration of 5 mg L^{-1}. The adsorption capacities of Fe-WTR and Al-WTR positively correlated with pH. The removal of Tl(I) using Fe-WTR exceeded Al-WTR; the adsorbed Tl(I) in Fe-WTR occurred primarily in the reduced state, while the Tl(I) adsorbed in Al-WTR was mainly in acid-extractable and reduced states. FTIR and XPS data showed that Tl(I) and Fe/Al-OH-functional groups formed stable surface complexes (Fe/Al-O-Tl) during adsorption, and there was no redox reaction. This confirmed that WTR is a highly efficient adsorbent for the stable removal of Tl(I), which provides a practical foundation for industrial application in Tl(I)-containing wastewater treatment.

Keywords: adsorption; thallium; Al-WTR; Fe-WTR; wastewater treatment

Citation: Xu, Y.; Qing, Y.; Gu, R.; Zhou, S.; Fu, G.; Zhao, Y. Efficient Adsorption of Tl(I) from Aqueous Solutions Using Al and Fe-Based Water Treatment Residuals. *Processes* **2022**, *10*, 2700. https://doi.org/10.3390/pr10122700

Academic Editor: Avelino Núñez-Delgado

Received: 9 November 2022
Accepted: 10 December 2022
Published: 14 December 2022

1. Introduction

Aquatic ecosystem pollution, especially heavy metal ion pollution, is a worldwide environmental problem. Thallium (Tl) is extremely poisonous and classified as a dangerous pollutant in China and the US. It is also a carcinogen with higher toxicity than lead, cadmium, and mercury [1–6], and readily enters and accumulates in humans via drinking water, food, and respiration, and results in disease and disorders [7,8]. Compared with other harmful elements, such as Cd, Pb, and Hg, Tl pollution receives much less attention [9–13]. As a component of coal and certain metal sulfide ores, thallium wastewater production comes from numerous anthropogenic activities, such as mining, smelting, and other industrial processes, and results in serious water pollution [14–19]. Thallium pollution plays a significant role in the environment and society, particularly in China. For example, the Hejiang River in Guangxi in 2013, the Jialing River in Sichuan in 2017, and the Lujiang River in Hunan in 2018 all experienced serious water Tl pollution, and negatively impacted the health of residents in those areas [20–22]. Tl(I) and Tl(III) are the two more common oxidation states of thallium. Tl(I) has high solubility and fluidity in aqueous solutions; therefore, most thallium found in wastewater occurs as Tl(I) [23]. However, Tl(I) is a toxic trace and mobile contaminant that does not readily adsorb many natural materials [24,25]. Therefore, it is urgent and essential to explore Tl(I)-containing wastewater treatment methods.

Tl(I) can be removed from wastewater in a variety of ways [26], including precipitation [27], solvent extraction [28,29], and electrochemical deposition [30,31]. These approaches suffer from removal efficiency, high operating costs, and high energy consumption. Recently, a high-efficiency, low-cost, and easy-to-operate adsorption method shown great

potential. Various adsorbents, such as carbon foam [32], activated carbon [33], nanoparticles [34], graphene derivatives [35], and many wastes materials, such as biomass [36] and water treatment residues (WTRs) [37], have been used to adsorb and remove heavy metals. Therefore, the adsorption method was considered one of the better treatment technologies for Tl(I)-containing wastewater [38–42], and the current research has focused on finding efficient, inexpensive Tl(I) adsorbents. At present, there have been many studies on Tl(I) adsorption removal using Prussian blue analogues, biological adsorbents, nanoparticles, and metal oxides [43]. However, these adsorptions have low Tl(I) selectivity, and coexisting cations readily interfere with Tl(I) removal [44]. Water treatment residuals (WTR) were considered to be the most effective heavy metal adsorbent, which are characterized by good adsorption properties [45], but their adsorption capacity is also affected by the adsorption conditions, such as pH, temperature, and time [46]. Previous studies have shown that WTRs do not release metals, which implies that they are nontoxic wastes and efficient adsorbents [47,48]. They reduce the cost of removing metals from water and also help reduce the amount of residue that accumulates in the environment [49]. WTRs are by-products formed during water purification. Different coagulants and flocculants added during water treatment can be divided into two distinct types, Fe-WTR, and Al-WTR [50,51], and these residuals have excellent adsorption properties due to the presence of amorphous aluminum/iron hydroxides, and have the advantages of easy availability, local materials, and large quantities of use [52]. In recent years, an increasing number of studies have been devoted to the use of WTRs to remove heavy metal from aqueous solutions. WTRs have been proven to be effective in removing heavy metals, such as As, Hg, Ni, Cu, and Pb [53–55]. For the past few years, most of the research is focused on the precipitation of phosphorus in wastewater [56–58]. Nevertheless, there are no reports of removing trace Tl(I) using WTR adsorption. Therefore, such research clearly merits examination for the treatment of Tl pollution in aqueous systems to utilize WTR resources more efficiently and to lower the cost of metal removal from water.

In this study, adsorption of Tl(I)-containing aqueous solutions was investigated using Al-based water treatment residuals (Al-WTR) and Fe-based water treatment residuals (Fe-WTR). A modified BCR sequential extraction method and batch experiments investigated the effects of pH on Tl(I) adsorption. Furthermore, the mechanisms of Tl(I) adsorption by Fe-WTR and Al-WTR were proposed based on FT-IR and XPS analyses.

2. Materials and Methods

2.1. Materials

Fe-WTR samples were collected from a water supply plant in Beijing, China; the coagulants used were polyferric sulfate and polyaluminum chloride. The samples of Al-WTR came from a water supply plant in Changsha, China; the coagulants used were polyaluminum chloride and the flocculant was polyacrylamide. At 105 °C, the dewatered sludge was dried to a constant weight. After grinding, the sludge was passed through a 0.15 mm sieve. $TlNO_3$ standard reagent (1000 mg L^{-1}) was diluted with ultra-pure water to prepare a thallium(I) stock solution. This study prepared a series of diluted Tl(I) solutions, and the pH was adjusted using solutions with different HNO_3 and NaOH concentrations. Sinopharm Chemical Reagent Co., Ltd. (Shanghai, China) provided all the analytical grade reagents used in this experiment.

2.2. WTR Characterization

Tl levels were determined by inductively coupled plasma mass spectrometry (ICP-MS, ICAP-RQ, Thermo, Waltham, MA, USA). Energy dispersive X-ray spectroscopy (EDS, Octane Elect, EDAX, Pleasanton, CA, USA) estimated the elemental compositions of the Al-WTR and Fe-WTR. WTR surface areas, pore sizes, and pore volumes were analyzed through N_2 adsorption–desorption using a Surface Area and Pore Size Analyzer (BET, 3Flex, Micromeritics, Norcross, GA, USA). Fourier transform infrared spectroscopy analyses indicated the WTR-surface-functional groups (FTIR, Nicolet iS50, Thermo, USA). Elemental

oxidation states and functional groups of WTR were analyzed using X-ray photoelectron spectroscopy (XPS, ESCALAB 250XI, Thermo, USA) with Al Kα (excitation X-ray source) operated at a 1486.6 eV pass energy. These results were fit using Thermo Avantage v5.9921. Zeta potentials of WTR at different pH values (3–9) were measured by a Zetasizer Nano ZS (ZEN 90, Malvern, UK).

2.3. Batch Adsorption Experiments

Kinesthetic adsorption experiments determined the effect of contact time on Tl(I) adsorption by WTR. The Tl(I) stock solution was diluted to 0.5 mg L^{-1}, and the pH was adjusted to 7.0 using HNO_3 and/or NaOH. A sample was mixed with WTR at a solid–liquid ratio of 2:5, and the solution was shaken in a centrifuge tube at 25 °C and 180 rpm. At 0, 2, 5, 10, 15, 20, 40, 60, 120, 240, 360, and 420 min, the suspensions were filtered through 0.45 µm microporous membrane filters. Tl concentrations in the filtrate were determined by ICP-MS. Each group of experiments was performed in triplicate.

Research results were fit using pseudo-first-order and pseudo-second-order kinetic models to understand the adsorption kinetics of Tl(I) by the two WTR types and provide insight into the adsorption mechanisms, see Equations (1) and (2) below [59,60].

$$\ln (q_e - q_t) = \ln q_e - k_1 t \quad (1)$$

$$\frac{t}{q_t} = \frac{1}{k_2 q_e^2} + \frac{t}{q_e} \quad (2)$$

where q_e (mg g^{-1}) and q_t (mg g^{-1}) are the adsorption capacity of the WTR at adsorption equilibrium and at time t; k_1 (min^{-1}); and k_2 (g mg^{-1} min^{-1}) are the rate constant of the two models, respectively.

Adsorption isotherm experiments were performed in 50 mL centrifuge tubes containing 50 mL of Tl(I) solution and 0.02 g WTR. Initial Tl(I) solution concentrations spanned 0.05, 0.1, 0.3, 0.5, 1, 3, and 5 mg L^{-1} at a constant pH of 7.0. The mixed solution was shaken at 25 °C and 180 rpm for 8 h, then filtered through 0.45 µm microporous membrane filters. The concentrations of Tl in the filtrates were determined using ICP-MS.

Langmuir and Freundlich isotherm models (Equations (3) and (4)) fit the adsorption isotherms of Tl(I) [61,62] to analyze the Tl(I) interactions with both WTR types. R_L quantified the adsorbent effectiveness and it was calculated using Equation (5) [63].

$$\frac{c_e}{q_e} = \frac{1}{q_{max} K_L} + \frac{c_e}{q_{max}} \quad (3)$$

$$\ln q_e = \ln K_F + \frac{1}{n} \ln c_e \times \ln q_e \quad (4)$$

$$R_L = \frac{1}{1 + K_L C_0} \quad (5)$$

where c_e (mg L^{-1}) is the equilibrium Tl concentration, q_{max} (mg g^{-1}) is the maximum saturated adsorption capacity of WTR, K_L (L mg^{-1}) is the Langmuir adsorption equilibrium constant, R_L is the Langmuir adsorption isotherm model and dimensionless separation factor, K_F and n are the Freundlich model constants.

2.4. Factors Affecting Tl(I) Sorption

Adsorption characteristics were affected primarily by the solution's pH. A $TlNO_3$ standard was used to prepare a 0.5 mg L^{-1} stock solution with ultra-pure water as a blank control group, and the pH levels adjusted to 3.0, 4.0, 5.0, 6.0, 7.0, 8.0, and 9.0, followed by mixing with 0.02 g WTR and shaking for 8 h at 25 °C and 180 rpm. ICP-MS detected the Tl concentration in the filtrate and the leached Al in WTR after 0.45 µm microporous membrane filters.

The effect of MPA dosage was also tested using a 0.5 mg L^{-1} Tl(I) stock solution at a pH of 7. WTR samples (0.02 g) were added to the solution after adjusting the solid–liquid

ratios to 2:8, 2:7, 2:6, 2:5, 2:4, 2:3, and 2:2 g L^{-1}. The mixed solutions were shaken for 8 h at 25 °C and 180 rpm. ICP-MS analyses determined Tl levels in the filtrate.

2.5. Modified BCR Sequential Extraction

Different concentrations of Tl(I) solution (10, 20, 30, and 40 mg L^{-1}) were mixed with 2.0 g Al-WTR and Fl-WTR separately by using 50 mL-centrifuge tubes. After shaking for 8 h (25 °C, 180 rpm), all samples were centrifuged with 8000 rpm at 25 °C. The sediment was air-dried to constant weight, followed by grinding and passing through a 0.15 mm sieve. A modified BCR sequential extraction procedure was used for the extraction of Tl form in the sifted samples [64,65].

3. Results and Discussion

3.1. Al-WTR and Fe-WTR Characterization

Table 1 shows the basic physical and chemical properties of Fe-WTR and Al-WTR. The characterization results of element content suggested that the Fe-WTR and Al-WTR were mainly composed of Al, Fe, C, O, and Ca. Due to the addition of polyferric sulfate, the concentration of Fe in Fe-WTR was higher than Al-WTR, and the addition of polyacrylamide increased C in Al-WTR. The results of BET showed the specific surface area and pore volume, and the average pore sizes for Fe-WTR and Al-WTR were 66.65 m^2 g^{-1}, 0.107 cm^3 g^{-1}, 5.76 nm, and 21.52 m^2 g^{-1}, 0.074 cm^3 g^{-1}, 10.29 nm, respectively.

Table 1. Fe-WTR and Al-WTR basic physical and chemical properties.

Sample	Specific Surface Area (m^2 g^{-1})	Pore Volume (cm^3 g^{-1})	Average Pore Size (nm)	Weight (%)							
				C	O	Al	Si	Fe	Mg	K	Ca
Al-WTR	21.52	0.074	10.29	15.20	44.45	15.58	16.91	3.82	1.41	1.52	0.76
Fe-WTR	66.65	0.107	5.76	6.54	43.05	10.09	18.52	13.36	0.98	0.38	6.45

3.2. Tl(I) Adsorption Kinetics and Isotherms

Figure 1 shows the Fe-WTR and Al-WTR adsorption kinetics for Tl(I). The adsorption of Tl(I) by Fe-WTR and Al-WTR occurred rapidly from 0–10 min. The absorptivities of Fe-WTR and Al-WTR both rapidly increased to more than 95% of the equilibrium adsorption capacity. This suggested that the adsorption of Tl(I) depended on many effective binding sites on Fe-WTR and Al-WTR surfaces. The adsorption equilibrium of Fe-WTR and Al-WTR for Tl(I) occurred within 120 min. After this time, the active adsorption sites on Fe-WTR and Al-WTR were saturated, which indicated that the systems reached equilibrium.

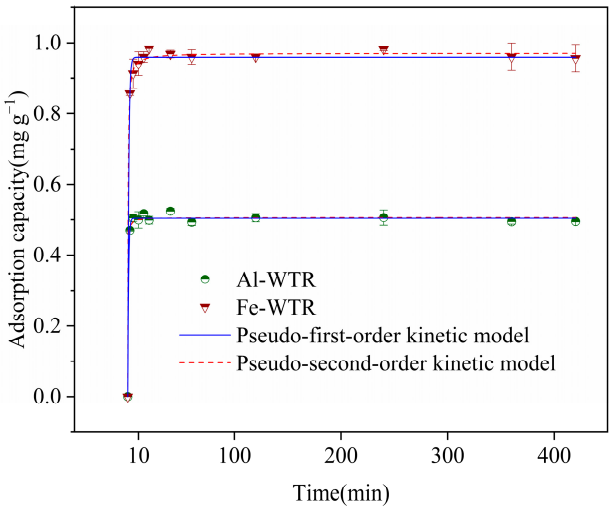

Figure 1. Kinetics of adsorption of Tl(I) by Fe-WTR and Al-WTR.

Experimental data were fit to pseudo-first-order and pseudo-second-order kinetic models as shown in Table 2. Both kinetic models fit the kinetics of Fe-WTR and Al-WTR adsorption of Tl(I), and the correlation coefficients R_1^2 and R_2^2 obtained surpassed 0.990. Regarding the simulated adsorption capacities, the pseudo-primary adsorption capacity was 0.959 mg g^{-1} and the pseudo-secondary adsorption capacity was 0.971 mg g^{-1} for Fe-WTR, which approximated the empirical data (0.956 mg g^{-1}). Furthermore, the simulated adsorption capacities acquired by pseudo-first-order and pseudo-second-order (0.504 and 0.506 mg g^{-1} for Al-WTR) approximated the empirical data (0.495 mg g^{-1} for Al-WTR). Therefore, the adsorbent process of Tl(I) by Fe-WTR and Al-WTR may include both physical and chemical adsorption. This indicated solid–liquid interface adsorption reactions and intraparticle diffusion during the adsorption of Tl(I) on Fe-WTR and Al-WTR [66]. Adsorbent diffusion through the solution to the outer surface of the adsorbent (out-diffusion) was readily accessible at the outer surface position and led to the first rapid adsorption. The second part involved intra-particle diffusion. Because adsorbed ions diffuse through the surface into the pores inside the adsorbent, the diffusion rate is low. Moreover, diffusion is slow because all binding sites are saturated [67,68]. A similar explanation was given for the adsorption of Pb and Cu using WTR containing polyaluminum chloride and anionic polyacrylamide [46].

Table 2. Adsorption kinetic model parameters of Fe-WTR and Al-WTR for Tl(I).

WTR	C_0 (mg L^{-1})	First-Order			Second-Order		
		q_e (mg g^{-1})	k_1 (min^{-1})	R_1^2	q_e (mg g^{-1})	k_2 (g mg^{-1} min^{-1})	R_2^2
Al-WTR	0.500	0.504	1.360	0.996	0.506	16.330	0.994
Fe-WTR	0.500	0.959	1.100	0.996	0.971	3.860	0.998

The isotherm adsorption curves of Fe-WTR and Al-WTR for Tl(I) are shown in Figure 2, and the fitting results obtained by Langmuir and Freundlich adsorption isotherm models are given in Table 3. The Langmuir model fits the Tl(I) process of Al-WTR adsorption better than the Freundlich model. Conversely, the Freundlich model better suits the Tl(I) adsorption of Fe-WTR than the Langmuir model. R^2 values in the Langmuir model for Fe-WTR and AL-WTR adsorptions were 0.954 and 0.963, respectively, compared with 0.993 and 0.958 in the Freundlich model. In fact, the R^2 values for the two isotherm adsorption models exceeded 0.950. This indicated that both models explain Tl(I) adsorption. The adsorption of Tl(I) has monolayer and multilayer adsorption [69,70].

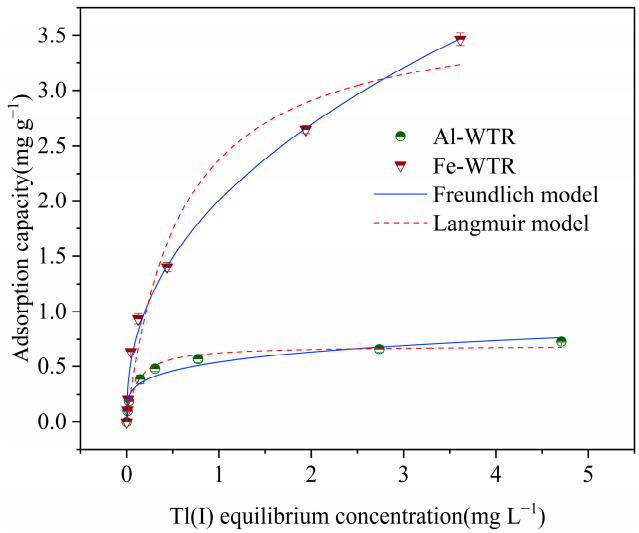

Figure 2. Isothermal adsorption model of Fe-WTR and Al-WTR for Tl(I).

Table 3. Isothermal adsorption model parameters of Fe-WTR and Al-WTR for Tl(I).

WTR	Langmuir			Freundlich		
	q_{max} (mg g^{-1})	K_L (L mg^{-1})	$R_L{}^2$	n	K_F	$R_F{}^2$
Al-WTR	0.690	9.120	0.963	4.300	0.530	0.958
Fe-WTR	3.751	1.720	0.954	2.340	2.000	0.993

In the Langmuir model, the adsorption equilibrium constants K_L of Fe-WTR and Al-WTR were 1.720 and 9.120, respectively, which indicated that adsorption of Tl(I) by Fe-WTR and Al-WTR proceeded spontaneously at room temperature. The separation factors $R_L{}^2$ of Fe-WTR and Al-WTR were 0.954 and 0.963, respectively, which satisfied the condition of $0 < R_L < 1$ and showed that both Fe-WTR and Al-WTR favored Tl(I) adsorption [71]. At 5 mg L^{-1}, the maximum saturated adsorption capacities of Fe-WTR and Al-WTR were 3.751 mg g^{-1} and 0.690 mg g^{-1}, respectively, which indicated that Fe-WTR adsorbed Tl(I) better than Al-WTR. In the Freundlich model, the corresponding n values for Al-WTR and Fe-WTR were 4.300 and 2.340, respectively, which satisfied the $n > 2$ condition, which indicated that both Fe-WTR and Al-WTR have good adsorption properties for Tl(I) [72]. Higher K_F values indicate higher adsorption capacities for Tl(I). The corresponding K_F values of Al-WTR and Fe-WTR were 0.530 and 2.000, respectively, which indicated that Fe-WTR had higher adsorption relative to Al-WTR. The adsorption capacities of Fe-WTR, Al-WTR and other adsorbents were compared and listed in Table 4.

Table 4. Comparison of adsorption capacity of Fe-WTR and Al-WTR with other adsorbents.

Sorbents	Maximum Adsorption Capacity (mg g^{-1})	References
Treated sawdust	13.18	[69]
nano-Al_2O_3	6.3	[73]
Waste pomelo biochar	4.2839	[74]
Pomelo peel biochar	5.2860	[74]
Walnut shells	0.985	[75]
Modified Aspergillus niger biomass	0.186	[76]
Watermelon rinds biochar	178.4	[77]
Multiwalled carbon nanotube	0.42	[78]
Nano-TiO_2	51.2	[79]
Fe_3O_4@PB	528	[80]
Manganese oxide nanoparticle	505.5	[39]
Al-WTR	0.690	This work
Fe-WTR	3.751	This work

3.3. Effect of Solution pH and Dosage

Figure 3 shows the effects of pH on Fe-WTR and Al-WTR Tl(I) adsorption. The adsorption capacities of Fe-WTR and Al-WTR gradually increased as the pH increased. The adsorption capacities of Fe-WTR and Al-WTR were 0.875 mg g^{-1} and 0.279 mg g^{-1}, respectively, at pH 3. As the pH increased to nine, the adsorption capacities of Fe-WTR and Al-WTR increased to 1.030 mg g^{-1} and 0.704 mg g^{-1}. The solution pH affected the WTR surface charge [51]. As shown in Figure 4, Fe-WTR and Al-WTR had isoelectric points of 3.05 and 3.97, respectively. The positive surface charge of Al-WTR decreased with increasing pH at $pH < pH_{pzc}$, and the negative surface charge increased as the pH increased to $pH > pH_{pzc}$. This was attributed to oxygen-functional groups on the adsorbent surface [81,82]. Therefore, at a pH of three, protonation of –OH-functional groups on Fe-WTR and Al-WTR increased the positive charge on the WTR surface. This enhanced electrostatic repulsions with the Tl(I) ion, which resulted in lower adsorption capacities for both WTRs. Conversely, the deprotonation degree of Fe-WTR and Al-WTR surfaces

enhanced at pH > 3 and increased negative charges on the WTR surface. Electrostatic attractions between WTR and Tl(I) increased, which increased Tl(I) adsorption.

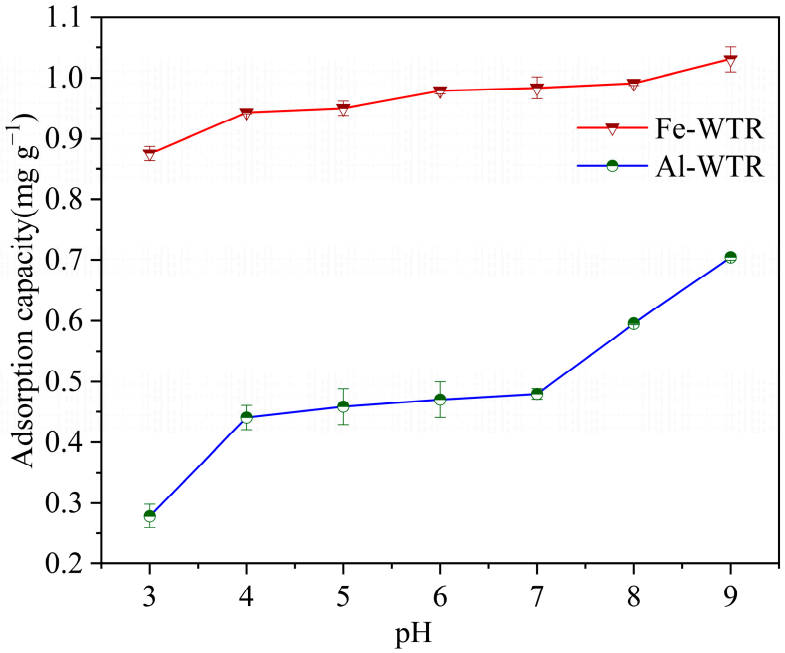

Figure 3. Effect of Fe-WTR and Al-WTR on Tl(I) adsorption under different pH conditions.

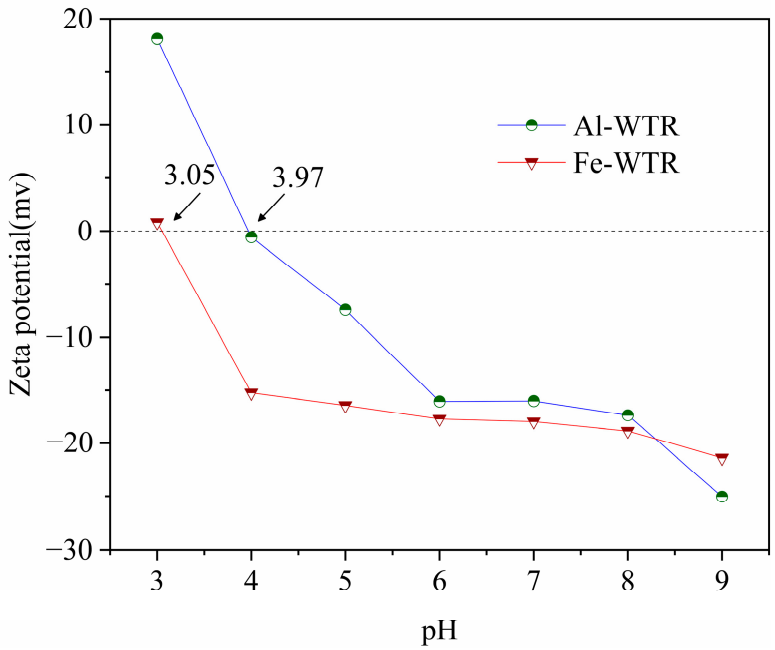

Figure 4. Zeta potential diagram of Fe-WTR and Al-WTR.

Although most studies consider WTR to be harmless [48] as a residue given to water plants, it contains more aluminum than most of the other metal components it contains, thus, posing a potential risk of aluminum contamination in applications [59]. From this, the influence of Fe-WTR and Al-WTR on the leaching of Al from Tl(I) solution and ultra-pure water under different pH conditions was compared, and the results are shown in Figure 5. The results show that the leaching concentration of Al in Fe-WTR and Al-WTR is related to the pH of the solution. The leaching concentration of Al in Al-WTR was less than 0.2 mg L^{-1} in both ultra-pure water with pH 4–8 and the Tl(I) solution with pH 4–9, which

has achieved the Chinese standard for drinking water (0.20 mg L^{-1}, GB5749-2006) [52]. Similarly, the leaching concentration of Al in Fe-WTR is only less than 0.2 mg/L at pH 3 but higher than 0.2 mg/L at pH 4–9 in both ultra-pure water and Tl(I) solution.

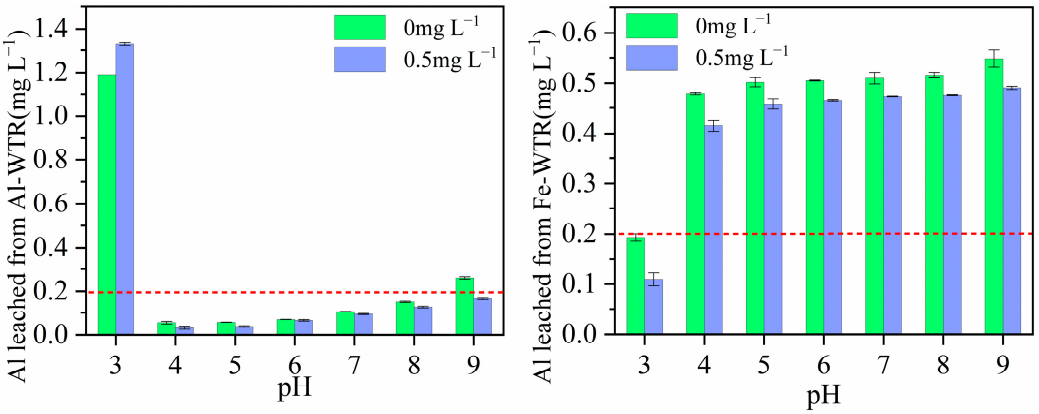

Figure 5. Effect of different pH conditions on the leaching of Al in Fe-WTR and Al-WTR.

Figure 6 shows the Tl(I) adsorption and removal rate for Fe-WTR and Al-WTR. The removal rates of Fe-WTR and Al-WTR increased from 67.74% to 91.89% and from 34.60% to 68.59%, respectively, as the solid–liquid ratio increased from 2:8 to 2:2 g L^{-1}. The adsorption capacity of Fe-WTR and Al-WTR separately decreased from 1.355 to 0.459 mg g^{-1} and from 0.692 to 0.343 mg g^{-1}. Removal rates of Fe-WTR and Al-WTR both increased with solid–liquid ratio increases, while the adsorption amount decreased with solid–liquid ratio increases. Among them, the increased removal rate was caused by increased surface areas and adsorbable active sites for Fe-WTR and Al-WTR. However, the adsorption decrease was due to an increase of unsaturated active sites per unit mass of Fe-WTR and Al-WTR [70]. Under identical solid–liquid ratios, Fe-WTR had a greater adsorption amount and removal rate than t Al-WTR. This may be caused by Fe-WTR having a more abundant surface pore structure. This was confirmed by Fe-WTR (Table 1) BET analysis results.

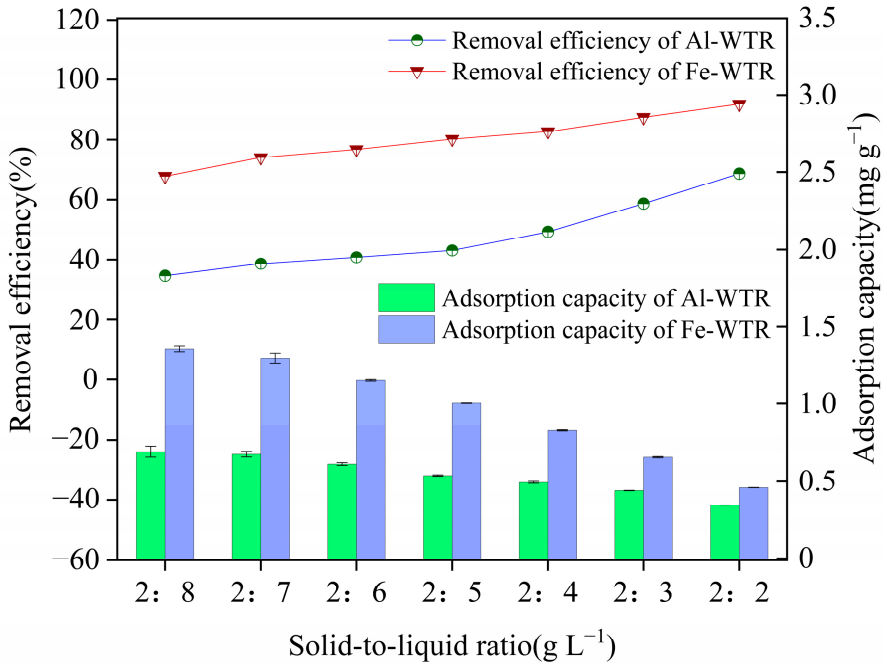

Figure 6. Effects of different solid–liquid ratios on adsorption of Tl(I) by Fe-WTR and Al-WTR.

3.4. Forms of Tl under Adsorption

Figure 7 shows the fractional extraction Tl results in Fe-WTR and Al-WTR after adsorption by modified BCR. The forms of Tl in Fe-WTR and Al-WTR after adsorption were divided into the following four categories: (1) Acid-exchangeable (moiety bound to carbonate, dissolved salt, or exchangeable ion); (2) Reducible state (the part bound to iron manganese oxides); (3) Oxidizable state (the part bound to organic matter or sulfide); (4) Residual state (the part bound to silicate) [83,84]. Among those categories, the acid-exchangeable state readily migrated and transformed in the environment; however, the reducible, residue, and oxidizable states were less likely to migrate and transform [85].

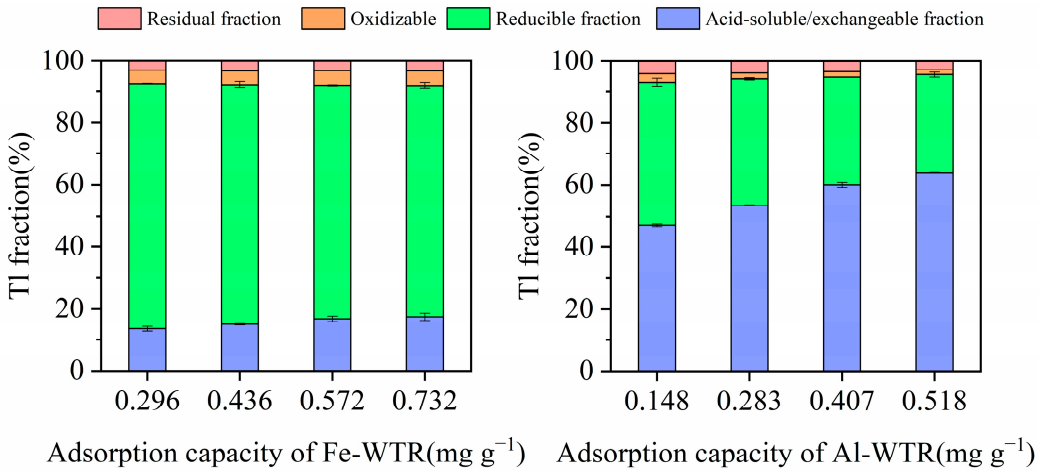

Figure 7. Occurrence forms of Tl(I) elements adsorbed by Fe-WTR and Al-WTR under different adsorption.

When the adsorption of Tl(I) on Al-WTR increased from 0.148 mg g^{-1} to 0.518 mg g^{-1}, the ratio of acid-exchangeable Tl increased significantly (from 47% to 64%). However, the proportion of the reducible state has decreased from 46% to 32%. The proportions of oxidizable and residue states changed little (from 3 to 2% and 4 to 3%, respectively). Moreover, as the adsorption of Tl(I) by Fe-WTR increased from 0.296 mg g^{-1} to 0.732 mg g^{-1}, the proportions of the four types of Tl were relatively small. The proportion of exchangeable and oxidizable states increased moderately (from 13 to 17% and 4 to 5%). The proportion of the reducible state decreased from 79 to 75%, and the residue state remained basically unchanged. The differences in Tl morphology may relate to the grain size and crystallization effect of Fe-WTR and Al-WTR [86]. The existing form of Tl in Fe-WTR after adsorption was primarily the reducible state, which tends not to migrate or transform. However, the existing form of Tl in Al-WTR was mainly the acid-exchangeable, which readily migrates and transforms, though the reducible state less readily migrates or transforms. Fe-WTR has a higher reduction state for Tl adsorption than Al-WTR, while the acid-extractable state was lower than Fe-WTR at the same initial conditions. This indicated that Fe-WTR was superior to Al-WTR in terms of stability and chemisorption properties for removing Tl(I).

3.5. Possible Mechanisms of Tl(I) Adsorption

Figure 8 shows FTIR spectra used to evaluate functional group differences between Fe-WTR and Al-WTR before and after adsorption. The blank group (before adsorption) shows –OH stretching vibration peaks (3440 cm^{-1}) [87,88], –OH bending vibration peaks (1640 cm^{-1}) [54], and Al/Fe–O stretching vibration peaks (470 and 536 cm^{-1}) on the WTR surface [89–91]. In addition, the peaks at 1040 and 1080 cm^{-1} correspond to Al–OH bending vibrations [92,93]. By comparison, after Fe-WTR and Al-WTR adsorb Tl(I), the peak intensities of –OH stretching and bending vibrations decreased significantly, which indicated that –OH groups on the WTR surface participated in Tl(I) adsorption. The Al/Fe–O stretching vibration peak intensities weakened slightly, with the peak of Fe–O stretching

vibrations moving from 470 to 467 cm^{-1}, and the peak of Al–O stretching moving from 468 to 470 cm^{-1}. This indicated a strong interaction between Al/Fe–O metal oxide groups and Tl(I) [54]. This confirmed that the most critical active Tl(I) adsorption sites were the abundant –OH groups and Al/Fe–O groups on the Fe-WTR and Al-WTR surfaces. Studies have shown that the bending vibration of –OH was connected to the stretching vibration of Al/Fe–O [37]. This may stem from the complexation of Al/Fe–OH groups on Fe-WTR and Al-WTR surfaces, with Tl(I) forming Al–O–Tl or Fe–O–Tl complexes.

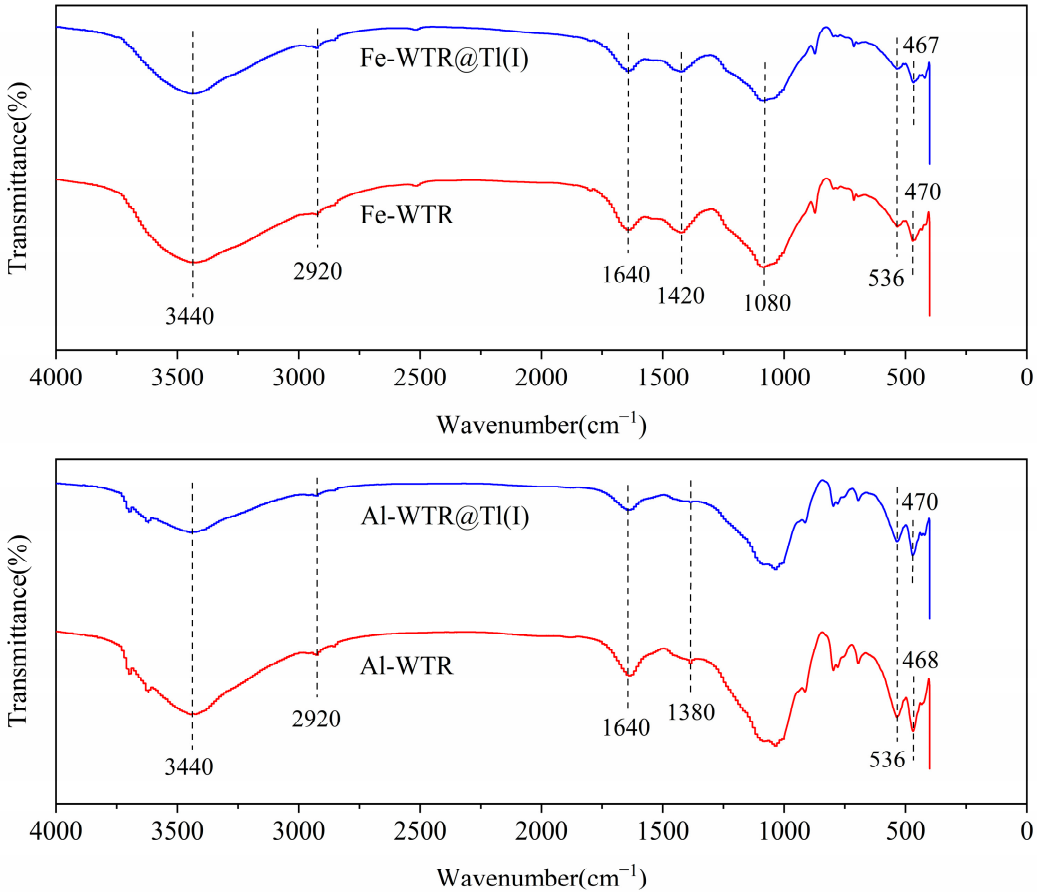

Figure 8. FTIR spectra of Fe-WTR and Al-WTR before and after adsorption.

Figures 9–11 show full XPS spectra, Tl 4f, and O 1 s XPS spectra of before and after Al-WTR and Fe-WTR adsorbed Tl(I). Both Fe-WTR and Al-WTR had a Tl 4f characteristic peak without spin splitting before adsorption, which was located at 119.02 eV and 118.98 eV, respectively, which was caused by the adsorption of trace Tl(I) in water during the process of water purification by water feeders. After the adsorption of Tl(I), two peaks were observed in Figure 10, which are generally defined as spin orbit splitting: Tl $4f_{7/2}$ and Tl $4f_{5/2}$, the spin-orbit splitting is 4.4 eV, with the bimodal energy of 119.31 eV, 123.7 eV and 119.04 eV, 123.5 eV, respectively. The distance between the two is 4.42 eV and 4.46 eV. It indicated successful loading of Tl(I) on Fe-WTR and Al-WTR [94,95]. The loaded Tl still exists as a cation (Tl^+), which confirmed that no redox reaction occurred during the Fe-WTR and Al-WTR removal of Tl(I).

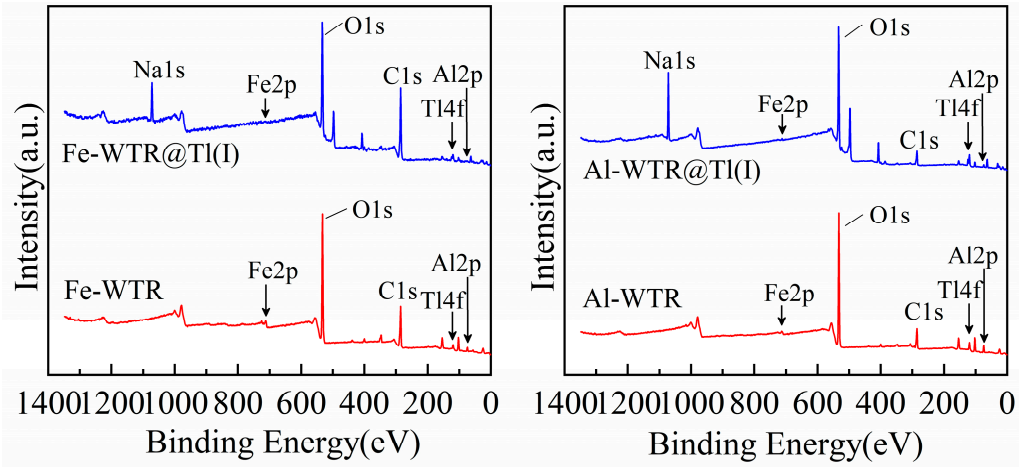

Figure 9. XPS spectra of Al-WTR and Fe-WTR before and after adsorption.

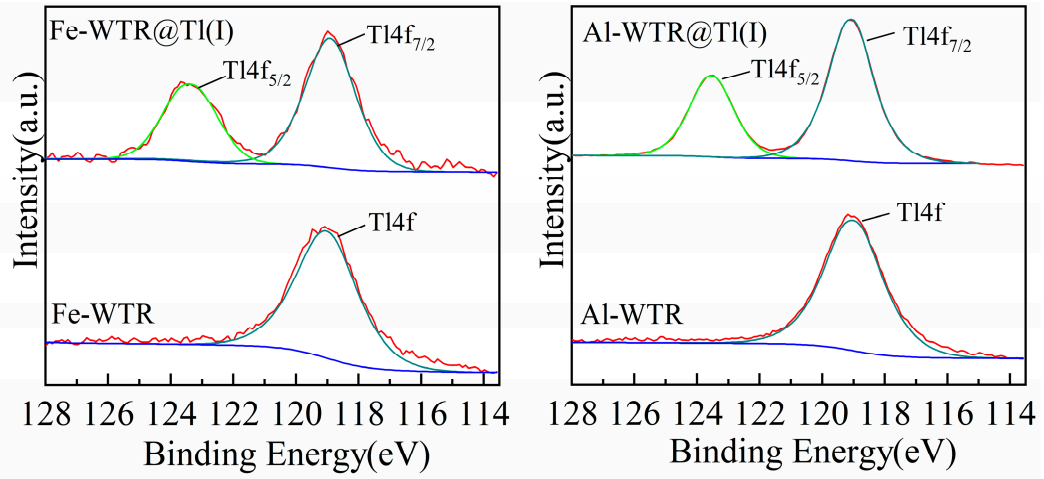

Figure 10. Tl 4f spectra of Al-WTR and Fe-WTR before and after adsorption.

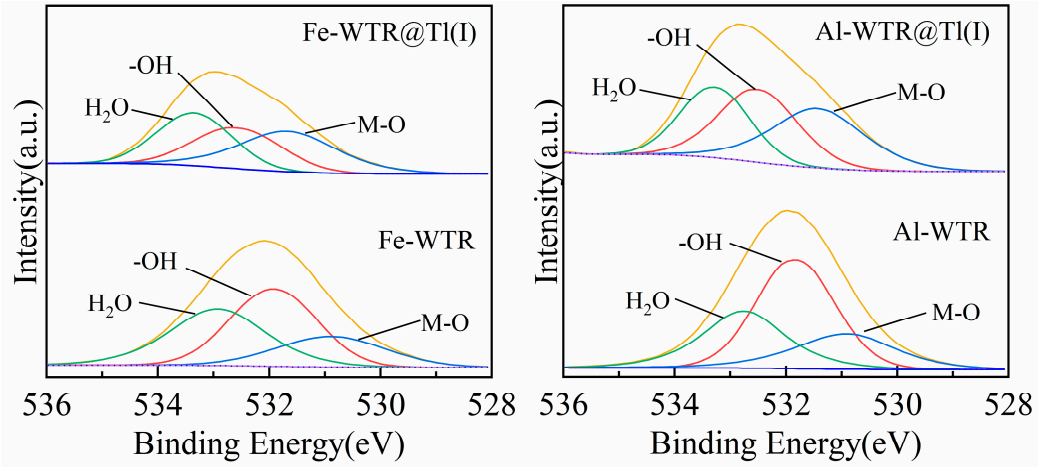

Figure 11. O 1 s spectra of Al-WTR and Fe-WTR before and after adsorption.

According to FTIR results (Figure 8), the functional groups of Fe-WTR and Al-WTR closely relate to Tl(I) adsorption. Therefore, the changes of oxygen-containing groups before and after adsorption were analyzed by measuring O 1 s XPS spectra. Three peaks with binding energies of 530.94, 531.82, and 532.76 eV were fit to the O 1 s peak prior to Al-WTR adsorption, which corresponded to metal–oxygen bond (M–O), hydroxyl (–OH)

and adsorbed water (H_2O), respectively [96,97]. After Tl(I) adsorption, metal–oxygen bond (M–O) levels increased from 21.80 to 34.75%, while hydroxyl (M–OH) levels decreased from 49.02 to 35.45%, and the adsorbed water levels increased from 29.18% to 29.80%, with binding energies of 531.42, 532.50 and 533.27 eV, respectively (Figure 11). Before adsorption, the O 1 s peak of Fe-WTR separated into three subpeaks with binding energies of 530.87, 531.92, and 532.94 eV, corresponding to metal–oxygen bonds, hydroxyl groups and adsorbed water [98,99]. After Tl(I) adsorption, metal–oxygen levels increased from 21.33 to 35.40%, hydroxyl levels decreased from 42.53 to 30.49%, and the adsorbed water levels increased from 36.14% to 34.11%, with binding energies of 531.67, 532.57, and 533.35 eV (Figure 11). After the adsorption of Tl(I) by Fe-WTR and Al-WTR, OH peak levels decreased significantly, while the content of M O peak increased significantly, and the oxidation state of Tl(I) remained intact. This confirmed the number of –OH and M–O group changes related directly to Tl(I) adsorption and indicated that adsorption may involve ion exchange of H^+ in the –OH group and Tl(I) to produce Fe–O–Tl or Al–O–Tl complexes [100,101].

Figure 12 shows a proposed mechanism of Fe-WTR and Al-WTR adsorption of Tl(I) inferred from these results and divided into three points.

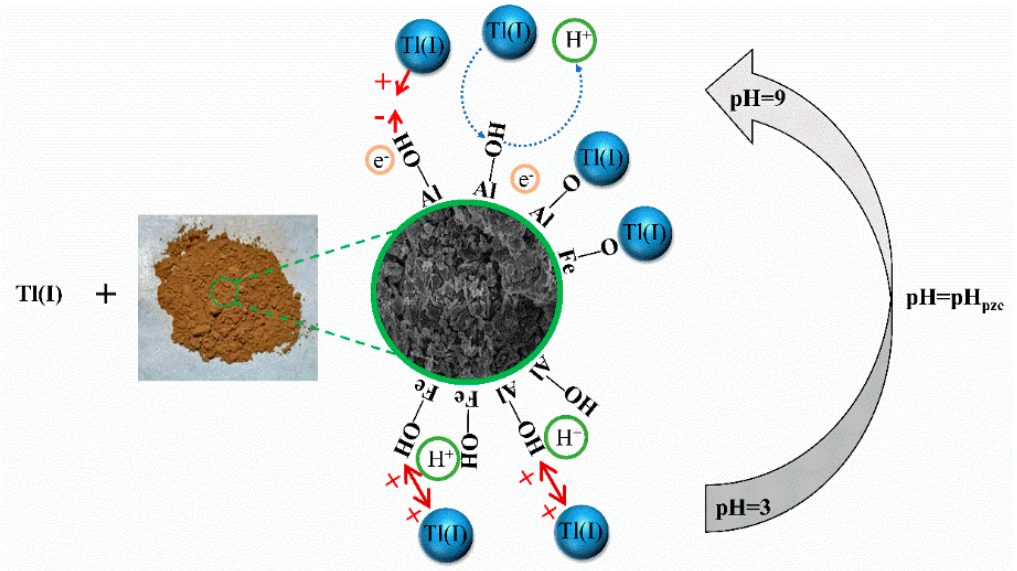

Figure 12. Mechanism diagram of Tl(I) adsorption by Al-WTR and Fe-WTR.

(1) Active adsorption sites. –OH groups that bind Fe/Al atoms.

(2) Electrostatic adsorption. Fe-WTR and Al-WTR surface charges react significantly to pH changes. Therefore, as the solution pH < pH_{pzc}, the Fe-WTR and Al-WTR surfaces were positively charged, and H^+ prevented Tl(I) from adhering to WTR by electrostatic repulsion. When the pH > pH_{pzc}, the Fe-WTR and Al-WTR surfaces were both negatively charged, which promoted electrostatic interactions between Tl(I) and WTR to accelerate Tl(I) adsorption to their surfaces.

(3) Ion exchange. During Tl(I) and H^+ ion exchange, a large amount of H^+ in solution competes with Tl(I) and inhibits Tl(I) adsorption by Fe-WTR and Al-WTR. Increasing the solution's pH enhanced the deprotonation of Fe-WTR and Al-WTR surfaces so that Tl(I) approaches Fe-WTR and Al-WTR surfaces to ionize the Fe–OH or Al–OH groups. After the exchange, a stable Fe–O–Tl or Al–O–Tl structure formed, which stabilized and removed Tl(I) from the water.

4. Conclusions

This paper reports the first example of the rapid and efficient adsorption of Tl(I) on Al-WTR and Fe-WTR. The adsorption kinetics showed that adsorption may involve both physisorption and chemisorption, and the adsorption equilibrium occurred within 120 min. The adsorption isotherms were fit using both Langmuir and Freundlich models. The Tl(I) adsorption capacity increased at higher pH but decreased at higher solid-to-liquid ratios. Favorable Tl(I) adsorption occurred when the solution pH > pH_{pzc}. The adsorbed Tl(I) in Fe-WTR was mainly in the reducible state, and the Tl(I) adsorbed in Al-WTR was mainly in the acid-exchangeable and reduced states. Fe-WTR exceeded Al-WTR in terms of stability and chemisorption for removing Tl(I). Active site adsorption, electrostatic interactions, ion exchange, and surface complexation were the primary mechanisms for removing Tl(I). Consequently, WTR is a promising and eco-friendly adsorbent that can help reduce Tl(I) pollution in aqueous solutions. This may provide a starting point for the development of a viable and cost-effective adsorption technology.

Author Contributions: Conceptualization, Y.X. and G.F.; methodology, Y.Z.; validation, Y.Q.; formal analysis, Y.X. and Y.Q.; investigation, Y.X., Y.Q. and R.G.; data curation, Y.X., Y.Q. and S.Z.; writing—original draft preparation, Y.X.; writing—review and editing, visualization, Y.X., Y.Q., R.G. and S.Z.; supervision, G.F.; project administration, G.F. and Y.Z.; funding acquisition, Y.Z. All authors have read and agreed to the published version of the manuscript.

Funding: This research was funded by the Key Research and Development Program of Hunan Province of China (No. 2019SK2291) and the Environmental Protection Research Project of Hunan Province (No. HBKT-2021023).

Data Availability Statement: Not applicable.

Conflicts of Interest: The authors declare no conflict of interest.

References

1. Asar, H.M.E.; Mohammed, E.A.; Aboulhoda, B.E.; Emama, H.Y.; Imam, A.A.A. Selenium protection against mercury neurotoxicity: Modulation of apoptosis and autophagy in the anterior pituitary. *Life Sci.* **2019**, *231*, 116578. [CrossRef] [PubMed]
2. She, J.; Liu, J.; He, H.; Zhang, Q.; Lin, Y.; Wang, J.; Yin, M.; Wang, L.; Wei, X.; Huang, Y. Microbial response and adaption to thallium contamination in soil profiles. *J. Hazard. Mater.* **2022**, *423*, 127080. [CrossRef] [PubMed]
3. Wang, J.; Zhou, Y.; Dong, X.; Yin, M.; Tsang, D.C.W.; Sun, J.; Liu, J.; Song, G.; Liu, Y. Temporal sedimentary record of thallium pollution in an urban lake: An emerging thallium pollution source from copper metallurgy. *Chemosphere* **2020**, *242*, 125172. [CrossRef] [PubMed]
4. Liu, J.; Li, N.; Zhang, W.; Wei, X.; Tsang, D.C.W.; Sun, Y.; Luo, X.; Bao, Z.A.; Zheng, W.; Wang, J. Thallium contamination in farmlands and common vegetables in a pyrite mining city and potential health risks. *Environ. Pollut.* **2020**, *248*, 906–915. [CrossRef] [PubMed]
5. Georgea, L.L.; Biagioni, C.; Lepore, G.O.; Lacalamita, M.; Agrosìc, G.; Capitani, G.C.; Bonaccorsi, E.; d'Acapito, F. The speciation of thallium in (Tl,Sb,As)-rich pyrite. *Ore Geol. Rev.* **2019**, *107*, 364–380. [CrossRef]
6. Puccini, M.; Guazzelli, L.; Tasca, A.L.; Mezzetta, A.; Pomelli, C.S. Development of a Chemosensor for the In Situ Monitoring of Thallium in the Water Network. *Water Air Soil Pollut.* **2018**, *229*, 239.
7. Wei, X.; Wang, J.; She, J.; Sun, J.; Liu, J.; Wang, Y.; Yang, X.; Ouyang, Q.; Lin, Y.; Xiao, T. Thallium geochemical fractionation and migration in Tl-As rich soils: The key controls. *Sci. Total Environ.* **2021**, *784*, 146995. [CrossRef]
8. Wei, X.; Zhou, Y.; Tsang, D.C.; Song, L.; Zhang, C.; Yin, M.; Liu, J.; Xiao, T.; Zhang, G.; Wang, J. Hyperaccumulation and transport mechanism of thallium and arsenic in brake ferns (*Pteris vittata* L.): A case study from mining area. *J. Hazard. Mater.* **2020**, *388*, 121756. [CrossRef]
9. Zhou, Y.; Wang, L.; Xiao, T.; Chen, Y.; Beiyuan, J.; She, J.; Zhou, Y.; Yin, M.; Liu, J.; Liu, Y. Legacy of multiple heavy metal(loid)s contamination and ecological risks in farmland soils from a historical artisanal zinc smelting area. *Sci. Total Environ.* **2020**, *720*, 137541.
10. Wang, J.; Jiang, Y.; Sun, J.; She, J.; Yin, M.; Fang, F.; Xiao, T.; Song, G.; Liu, J. Geochemical transfer of cadmium in river sediments near a lead-zinc smelter. *Ecotoxicol. Environ. Saf.* **2020**, *196*, 110529. [CrossRef]
11. Yin, M.; Tsang, D.C.W.; Wang, J.; Shang, J.; Fang, F.; Wu, Y.; Liu, J.; Song, G.; Xiao, T.; Chen, D. Critical insight and indication on particle size effects towards uranium release from uranium mill tailings: Geochemical and mineralogical aspects. *Chemosphere* **2020**, *250*, 126315. [PubMed]
12. Zeng, J.; Han, G. Preliminary copper isotope study on particulate matter in Zhujiang River, southwest China: Application for source identification. *Ecotoxicol. Environ. Saf.* **2020**, *198*, 110663. [CrossRef] [PubMed]

13. Zhong, Q.; Zhou, Y.; Tsang, D.C.W.; Liu, J.; Yang, X.; Yin, M.; Wu, S.; Wang, J.; Xiao, T.; Zhang, Z. Cadmium isotopes as tracers in environmental studies: A review. *Sci. Total Environ.* **2020**, *736*, 139585. [PubMed]
14. Vaněk, A.; Grösslová, Z.; Mihaljevič, M.; Trubač, J.; Ettler, V.; Teper, L.; Cabala, J.; Rohovec, J.; Zádorová, T.; Penížek, V. Isotopic Tracing of Thallium Contamination in Soils Affected by Emissions from Coal-Fired Power Plants. *Environ. Sci. Technol.* **2016**, *50*, 9864–9871. [CrossRef] [PubMed]
15. Li, N.; Zhou, Y.; Liu, J.; Tsang, D.C.W.; Wang, J.; She, J.; Zhou, Y.; Yin, M.; Chen, Z.; Chen, D. Persistent thallium contamination in river sediments, source apportionment and environmental implications. *Ecotoxicol. Environ. Saf.* **2020**, *202*, 110874.
16. Saleh, T.A.; Tuzen, M.; Sarı, A. Polyamide magnetic palygorskite for the simultaneous removal of Hg(II) and methyl mercury; with factorial design analysis. *J. Environ. Manag.* **2018**, *211*, 323–333. [CrossRef]
17. Mustafa, T.; Sarı, A.; Saleh, T.A. Response surface optimization, kinetic and thermodynamic studies for effective removal of rhodamine B by magnetic AC/CeO_2 nanocomposite. *J. Environ. Manag.* **2018**, *206*, 170–177.
18. Liu, J.; Wang, J.; Xiao, T.; Bao, Z.A.; Lippold, H.; Luo, X.; Yin, M.; Ren, J.; Chen, Y.; Linghu, W. Geochemical dispersal of thallium and accompanying metals in sediment profiles from a smelter-impacted area in South China. *Appl. Geochem.* **2018**, *88*, 239–246. [CrossRef]
19. Liu, J.; Yin, M.; Xiao, T.; Zhang, C.; Tsang, D.C.W.; Bao, Z.A.; Zhou, Y.; Chen, Y.; Luo, X.; Yuan, W. Thallium isotopic fractionation in industrial process of pyrite smelting and environmental implications. *J. Hazard. Mater.* **2020**, *384*, 121378. [CrossRef]
20. Liu, J.; Luo, X.; Sun, Y.; Tsang, D.C.W.; Qi, J.; Zhang, W.; Li, N.; Yin, M.; Wang, J.; Lippold, H. Thallium pollution in China and removal technologies for waters: A review. *Environ. Int.* **2019**, *126*, 771–790. [CrossRef]
21. Xu, H.; Luo, Y.; Wang, P.; Zhu, J.; Yang, Z.; Liu, Z. Removal of thallium in water/wastewater: A review. *Water Res.* **2019**, *165*, 114981. [CrossRef] [PubMed]
22. Liu, J.; Wang, J.; Tsang, D.C.W.; Xiao, T.; Chen, Y.; Hou, L. Emerging Thallium Pollution in China and Source Tracing by Thallium Isotopes. *Environ. Sci. Technol.* **2018**, *52*, 11977–11979. [CrossRef]
23. Liu, J.; Ren, S.; Cao, J.; Tsang, D.C.W.; Beiyuan, J.; Peng, Y.; Fang, F.; She, J.; Yin, M.; Shen, N. Highly efficient removal of thallium in wastewater by $MnFe_2O_4$-biochar composite. *J. Hazard. Mater.* **2021**, *401*, 123311.
24. Li, H.; Xiong, J.; Zhang, G.; Liang, A.; Long, J.; Xiao, T.; Chen, Y.; Zhang, P.; Liao, D.; Lin, L. Enhanced thallium(I) removal from wastewater using hypochlorite oxidation coupled with magnetite-based biochar adsorption. *Sci. Total Environ.* **2020**, *698*, 134166. [CrossRef] [PubMed]
25. Haris, M.; Usman, M.; Su, F.; Lei, W.; Saleem, A.; Hamid, Y.; Guo, J.; Li, Y. Programmable synthesis of exfoliated biochar nanosheets for selective and highly efficient adsorption of thallium. *Chem. Eng. J.* **2022**, *434*, 134842. [CrossRef]
26. Hosseini, M.S.; Chamsaz, M.; Raissi, H.; Naseri, Y. Flotation Separation and Electrothermal Atomic Absorption Spectrometric Determination of Thallium in Wastewater Samples. *Ann. Chim.* **2006**, *96*, 109–116. [CrossRef] [PubMed]
27. Dutrizac, J.E. The behaviour of thallium(III) during jarosite precipitation. *Metall. Mater. Trans. B* **1997**, *28*, 765–776. [CrossRef]
28. Escudero, L.B.; Wuilloud, R.G.; Olsina, R.A. Sensitive determination of thallium species in drinking and natural water by ionic liquid-assisted ion-pairing liquid–liquid microextraction and inductively coupled plasma mass spectrometry. *J. Hazard. Mater.* **2013**, *244–245*, 380–386. [CrossRef]
29. Rajesh, N.; Subramanian, M.S. A study of the extraction behavior of thallium with tribenzylamine as the extractant. *J. Hazard. Mater.* **2006**, *135*, 74–77. [CrossRef]
30. Kozina, S.A. Stripping Voltammetry of Thallium at a Film Mercury Electrode. *J. Anal. Chem.* **2003**, *58*, 954–958. [CrossRef]
31. Ussipbekova, Y.Z.; Seilkhanova, G.A.; Jeyabharathi, C.; Scholz, F.; Kurbatov, A.P.; Nauryzbaev, M.K.; Berezovskiy, A. Electrochemical Deposition and Dissolution of Thallium from Sulfate Solutions. *Int. J. Anal. Chem.* **2015**, *3*, 357514. [CrossRef] [PubMed]
32. Chang-Gu, L.; Jun-Woo, J.; Min-Jin, H.; Kyu-Hong, A.; Chanhyuk, P.; Jae-Woo, C.; Sang-Hyup, L. Lead and copper removal from aqueous solutions using carbon foam derived from phenol resin. *Chemosphere* **2015**, *130*, 59–65.
33. Panya, M.; Surachai, K. Adsorption behaviour of Fe(II) and Cr(VI) on activated carbon: Surface chemistry, isotherm, kinetic and thermodynamic studies. *J. Chem. Thermodyn.* **2016**, *106*, 104–112.
34. Joshi, N.C.; Rawat, B.S.; Kumar, P.; Kumar, N.; Upadhyay, S.; Chetana, S.; Gururani, P.; Kimothi, S. Sustainable synthetic approach and applications of ZnO/r-GO in the adsorption of toxic Pb^{2+} and Cr^{6+} ions. *Inorg. Chem. Commun.* **2022**, *145*, 110040. [CrossRef]
35. Joshi, N.C.; Rawat, B.S.; Semwal, P.; Kumar, N. Effective removal of highly toxic Pb^{2+} and Cd^{2+} ions using reduced graphene oxide, polythiophene, and silica-based nanocomposite. *J. Dispers. Sci. Technol.* **2022**, *28*, 2127752. [CrossRef]
36. Lingamdinne, L.P.; Yang, J.; Chang, Y.; Koduru, J.R. Low-cost magnetized Lonicera japonica flower biomass for the sorption removal of heavy metals. *Hydrometallurgy* **2016**, *165*, 81–89. [CrossRef]
37. Jiao, J.; Zhao, J.; Pei, Y. Adsorption of Co(II) from aqueous solutions by water treatment residuals. *J. Environ. Sci.* **2017**, *52*, 232–239. [CrossRef]
38. Kameda, T.; Ito, S.; Yoshioka, T. Kinetic and equilibrium studies of urea adsorption onto activated carbon: Adsorption mechanism. *J. Dispers. Sci. Technol.* **2017**, *38*, 1063–1066. [CrossRef]
39. Ren, Z.; Wu, W.; Yu, Y. Hydrothermal synthesis of needle-shaped manganese oxide nanoparticle for superior adsorption of thallium(I): Characterization, performance, and mechanism study. *Environ. Sci. Pollut. Res.* **2019**, *26*, 36776–36785. [CrossRef]
40. Chen, Z.; Zhang, S.; Liu, Y.; Alharbi, N.S.; Rabah, S.O.; Wang, S.; Wang, X. Synthesis and fabrication of g-C_3N_4-based materials and their application in elimination of pollutants. *Sci. Total Environ.* **2020**, *731*, 139054. [CrossRef]

41. Lin, L.; Song, Z.; Khan, Z.H.; Liu, X.; Qiu, W. Enhanced As(III) removal from aqueous solution by Fe-Mn-La-impregnated biochar composites. *Sci. Total Environ.* **2019**, *686*, 1185–1193. [CrossRef] [PubMed]
42. Zhou, Q.; Lin, L.; Qiu, W.; Song, Z.; Liao, B. Supplementation with ferromanganese oxide–impregnated biochar composite reduces cadmium uptake by indica rice (*Oryza sativa* L.). *J. Clean. Prod.* **2018**, *184*, 1052–1059. [CrossRef]
43. Hutapea, S.; Elveny, M.; Amin, M.A.; Attia, M.S.; Khan, A.; Sarkar, S.M. Adsorption of thallium from wastewater using disparate nano-based materials: A systematic review. *Arab. J. Chem.* **2021**, *14*, 103382. [CrossRef]
44. Zhao, Z.; Xiong, Y.; Cheng, X.; Hou, X.; Yang, Y.; Tian, Y.; You, J.; Xu, L. Adsorptive removal of trace thallium(I) from wastewater: A review and new perspectives. *J. Hazard. Mater.* **2020**, *393*, 122378. [CrossRef]
45. Likus, M.; Bajda, T. Current stage of knowledge telating to the use ferruginous sludge from eater treatment plants—A preliminary review of the literature. *Mineralogia* **2017**, *48*, 1–4.
46. Duan, R.; Fedler, C.B. Adsorptive removal of Pb^{2+} and Cu^{2+} from stormwater by using water treatment residuals. *Urban Water J.* **2021**, *18*, 237–247. [CrossRef]
47. Hovsepyan, A.; Bonzongo, J.-C.J. Aluminum drinking water treatment residuals (Al-WTRs) as sorbent for mercury: Implications for soil remediation. *J. Hazard. Mater.* **2009**, *164*, 73–80. [CrossRef]
48. Wang, C.; Yuan, N.; Pei, Y. Effect of pH on Metal Lability in Drinking Water Treatment Residuals. *J. Environ. Qual.* **2014**, *43*, 389–397. [CrossRef]
49. Wolowiec, M.; Komorowska-Kaufman, M.; Pruss, A.; Rzepa, G.; Bajda, T. Removal of heavy metals and metalloids from water using drinking water treatment residuals as adsorbents: A review. *Minerals* **2019**, *9*, 487. [CrossRef]
50. Wang, Q.; Shaheen, S.M.; Jiang, Y.; Li, R.; Slaný, M.; Abdelrahman, H.; Kwon, E.; Bolan, N.; Rinklebe, J.; Zhang, Z. Fe/Mn- and P-modified drinking water treatment residuals reduced Cu and Pb phytoavailability and uptake in a mining soil. *J. Hazard. Mater.* **2021**, *403*, 123628. [CrossRef]
51. Zhang, Z.; Sarkar, D.; Datta, R.; Yang, D. Adsorption of Perfluorooctanoic Acid (PFOA) and Perfluorooctanesulfonic Acid (PFOS) by Aluminum-based Drinking Water Treatment Residuals. *J. Hazard. Mater. Lett.* **2021**, *2*, 100034. [CrossRef]
52. Wang, M.; Bai, S.; Wang, X. Enhanced removal of heavy metals and phosphate in stormwater filtration systems amended with drinking water treatment residual-based granules. *J. Environ. Manag.* **2021**, *280*, 111645. [CrossRef] [PubMed]
53. Caporale, A.G.; Punamiya, P.; Pigna, M.; Violante, A.; Sarkar, D. Effect of particle size of drinking-water treatment residuals on the sorption of arsenic in the presence of competing ions. *J. Hazard. Mater.* **2013**, *260*, 644–651. [CrossRef]
54. Castaldi, P.; Silvetti, M.; Garau, G.; Demurtas, D.; Deiana, S. Copper(II) and lead(II) removal from aqueous solution by water treatment residues. *J. Hazard. Mater.* **2015**, *283*, 140–147. [CrossRef]
55. Ong, D.C.; Chi-Chuan, K.; Pingul-Ong, S.M.B.; Luna, M.D.G.D. Utilization of groundwater treatment plant (GWTP) sludge for nickel removal from aqueous solutions: Isotherm and kinetic studies. *J. Environ. Chem. Eng.* **2017**, *5*, 5746–5753. [CrossRef]
56. Zohar, I.; Ippolito, J.A.; Massey, M.; Litaor, I.M. Innovative approach for recycling phosphorous from agro-wastewaters using water treatment residuals (WTR). *Chemophere* **2017**, *168*, 234–243. [CrossRef]
57. Zohar, I.; Ippolito, J.A.; Rose, N.B.; Litaor, M. Phosphorus pools in Al and Fe-based water treatment residuals (WTRs) following mixing with agro-wastewater—A sequential extraction study. *Environ. Technol. Innov.* **2020**, *18*, 100654. [CrossRef]
58. Shen, C.; Zhao, Y.; Li, W.; Yang, Y.; Liu, R.; Morgen, D. Global profile of heavy metals and semimetals adsorption using drinking water treatment residual. *Chem. Eng. J.* **2019**, *372*, 1019–1027. [CrossRef]
59. Ho, Y.S.; McKay, G. Sorption of dye from aqueous solution by peat. *Chem. Eng. J.* **1998**, *70*, 115–124. [CrossRef]
60. Ho, Y.S.; McKay, G. Pseudo-second order model for sorption processes. *Process Biochem.* **1999**, *34*, 451–465. [CrossRef]
61. Freundlich, H. Über die adsorption in lösungen. *Z. Phys. Chem.* **1906**, *57*, 385–470. [CrossRef]
62. Langmuir, I. The Adsorption of Gases on Plane Surfaces of Glass, Mica and Platinum. *J. Am. Chem. Soc.* **1918**, *40*, 345.
63. Jacobson, A.T.; Fan, M. Evaluation of natural goethite on the removal of arsenate and selenite from water. *J. Environ. Sci.* **2019**, *76*, 133–141.
64. Rauret, G.; López-Sánchez, J.F.; Sahuquillo, A.; Rubio, R.; Davidson, C.; Ure, A.; Quevauviller, P. Improvement of the BCR three step sequential extraction procedure prior to the certification of new sediment and soil reference materials. *J. Environ. Monit.* **1999**, *1*, 57–61.
65. Yang, C.; Chen, Y.; Peng, P.A.; Li, C.; Chang, X.; Xie, C. Distribution of natural and anthropogenic thallium in the soils in an industrial pyrite slag disposing area. *Sci. Total Environ.* **2005**, *341*, 159–172. [CrossRef]
66. Simonin, J.P. On the comparison of pseudo-first order and pseudo-second order rate laws in the modeling of adsorption kinetics. *Chem. Eng. J.* **2016**, *300*, 254–263.
67. Sewu, D.D.; Jung, H.; Kim, S.S.; Lee, D.S.; Woo, S.H. Decolorization of cationic and anionic dye-laden wastewater by steam-activated biochar produced at an industrial-scale from spent mushroom substrate. *Bioresour. Technol.* **2019**, *277*, 77–86. [CrossRef]
68. Yadav, S.; Asthana, A.; Singh, A.K.; Chakraborty, R.; Vidya, S.S.; Susan, M.A.B.H.; Carabineirod, S.A.C. Adsorption of cationic dyes, drugs and metal from aqueous solutions using a polymer composite of magnetic/β-cyclodextrin/activated charcoal/Na alginate: Isotherm, kinetics and regeneration studies. *J. Hazard. Mater.* **2021**, *409*, 124840.
69. Memon, S.Q.; Memon, N.; Solangi, A.R.; Memon, J. Sawdust: A green and economical sorbent for thallium removal. *Chem. Eng. J.* **2008**, *140*, 235–240.
70. Park, H.; Singhal, N.; Jho, E.H. Lithium sorption properties of HMnO in seawater and wastewater. *Water Res.* **2015**, *87*, 320–327.

71. Babatunde, A.O.; Zhao, Y.Q.; Burke, A.M.; Morris, M.A.; Hanrahan, J.P. Characterization of aluminium-based water treatment residual for potential phosphorus removal in engineered wetlands. *Environ. Pollut.* **2009**, *157*, 2830–2836. [CrossRef] [PubMed]
72. Mesquita, M.E.; Vieira e Silva, J.M. Preliminary study of pH effect in the application of Langmuir and Freundlich isotherms to Cu–Zn competitive adsorption. *Geoderma* **2002**, *106*, 219–234. [CrossRef]
73. Zhang, L.; Huang, T.; Zhang, M. Studies on the capability and behavior of adsorption of thallium on nano-Al_2O_3. *J. Hazard. Mater.* **2008**, *157*, 352–357. [CrossRef] [PubMed]
74. Gao, C.; Cao, Y.; Lin, J. Insights into facile synthesized pomelo biochar adsorbing thallium: Potential remediation in agricultural soils. *Environ. Sci. Pollut. Res.* **2020**, *27*, 22698–22707. [CrossRef] [PubMed]
75. Karbowska, B.; Konowal, E.; Zembrzuski, W. Sorption of Thallium on Walnut Shells and its Enhancement by the Lignosulfonate-Stabilized Gold Colloid. *Pol. J. Environ. Stud.* **2019**, *28*, 2151–2158. [CrossRef] [PubMed]
76. John, P.A.L.; Viraraghavan, T. Removal of thallium from aqueous solutions by modified Aspergillus niger biomass. *Bioresour. Technol.* **2008**, *99*, 618–625. [CrossRef] [PubMed]
77. Li, H.; Xiong, J.; Xiao, T. Biochar derived from watermelon rinds as regenerable adsorbent for efficient removal of thallium(I) from wastewater. *Process Saf. Environ. Prot.* **2019**, *127*, 257–266. [CrossRef]
78. Pu, Y.; Yang, X.; Zheng, H. Adsorption and desorption of thallium(I) on multiwalled carbon nanotubes. *Chem. Eng. J.* **2013**, *219*, 403–410. [CrossRef]
79. Zhang, W.; Wu, Y.; Wang, J. Adsorption of thallium(I) on rutile nano-titanium dioxide and environmental implications. *PeerJ* **2019**, *16*, 7. [CrossRef]
80. Zhang, H.; Qi, J.; Liu, F. One-pot synthesis of magnetic Prussian blue for the highly selective removal of thallium(I) from wastewater: Mechanism and implications. *J. Hazard. Mater.* **2022**, *423*, 126972. [CrossRef]
81. Badruddoza, A.Z.M.; Shawon, Z.B.Z.; Daniel, T.W.J.; Hidajat, K.; Uddin, M.S. Fe_3O_4/cyclodextrin polymer nanocomposites for selective heavy metals removal from industrial wastewater. *Carbohydr. Polym.* **2013**, *91*, 322–332. [CrossRef] [PubMed]
82. Elshamy, O.; Alazabawy, R.; Elazabawy, O.; Masoud, E.M. Synthesis and Characterization of Magnetite-Alginate Nanoparticles for Enhancement of Nickel and Cobalt Ion Adsorption from Wastewater. *J. Nanomater.* **2019**, *2019*, 6326012.
83. Gao, J.; Zhao, J.; Dong, C.; Wu, L.; Hu, P. Remediation of metal-contaminated paddy soils by chemical washing with $FeCl_3$ and citric acid. *J. Soils Sediments* **2018**, *18*, 1020–1028. [CrossRef]
84. Ure, A.M.; Quevauviller, P.; Muntau, H.; Griepink, B. Speciation of Heavy Metals in Soils and Sediments. An Account of the Improvement and Harmonization of Extraction Techniques Undertaken Under the Auspices of the BCR of the Commission of the European Communities. *Int. J. Environ. Anal. Chem.* **1993**, *51*, 135–151. [CrossRef]
85. Antić-Mladenović, S.; Frohne, T.; Kresovića, M.; Stärk, H.-J.; Savić, D.; Ličina, V.; Rinklebe, J. Redox-controlled release dynamics of thallium in periodically flooded arable soil. *Chemosphere* **2017**, *178*, 268–276. [CrossRef]
86. Elkhatib, E.; Mahdy, A.; Sherif, F.; Elshemy, W. Competitive Adsorption of Cadmium(II) from Aqueous Solutions onto Nanoparticles of Water Treatment Residual. *J. Nanomater.* **2016**, *2016*, 8496798. [CrossRef]
87. Huang, P.; Liang, Z.; Zhao, Z.; Cui, F. Synthesis of hydrotalcite-like compounds with drinking water treatment residuals for phosphorus recovery from wastewater. *J. Clean. Prod.* **2021**, *301*, 126976.
88. Nagara, V.N.; Sarkar, D.; Elzinga, E.J.; Rupali, D. Removal of heavy metals from stormwater runoff using granulated drinking water treatment residuals. *Environ. Technol. Innov.* **2022**, *28*, 102636. [CrossRef]
89. Duan, R.; Fedler, C.B. Polyaluminium Chloride and Anionic Polyacrylamide Water Treatment Residuals as a Sorbent for Cd^{2+} and Zn^{2+} in Soils. *Water Air Soil Pollut.* **2021**, *232*, 7. [CrossRef]
90. Lian, J.; Zhou, F.; Chen, B.; Yang, M.; Wang, S.; Liu, Z.; Niu, S. Enhanced adsorption of molybdenum(VI) onto drinking water treatment residues modified by thermal treatment and acid activation. *J. Clean. Prod.* **2019**, *244*, 118719. [CrossRef]
91. Likus, M.; Komorowska-Kaufman, M.; Pruss, A.; Zych, Ł.; Bajda, T. Iron-Based Water Treatment Residuals: Phase, Physicochemical Characterization, and Textural Properties. *Materials* **2021**, *14*, 3938. [CrossRef] [PubMed]
92. Li, X.; Cui, J.; Pei, Y. Granulation of drinking water treatment residuals as applicable media for phosphorus removal. *J. Environ. Manag.* **2018**, *213*, 36–46. [CrossRef]
93. Qiu, F.; Wang, J.; Zhao, D.; Fu, K. Adsorption of myo-inositol hexakisphosphate in water using recycled water treatment residual. *Environ. Sci. Pollut. Res.* **2018**, *25*, 29593–29604. [CrossRef] [PubMed]
94. Yang, Z.; Wu, W.; Yu, L.; Fan, X.; Yu, Y. Fabrication and characterization of magnetically responsive Fe_3O_4@TiO_2 core-shell adsorbent for enhanced thallium removal. *Environ. Sci. Pollut. Res.* **2020**, *27*, 30518–30529. [CrossRef] [PubMed]
95. Li, L.; Liu, C.; Ma, R.; Yu, Y. Rapid removal of thallium from water by a new magnetic nano-composite using graphene oxide for efficient separation. *Int. Biodeterior. Biodegrad.* **2021**, *161*, 105245. [CrossRef]
96. Zhou, Y.; Liu, S.; Liu, Y.; Tan, X.; Liu, N.; Wen, J. Efficient Removal 17-Estradiol by Graphene-Like Magnetic Sawdust Biochar: Preparation Condition and Adsorption Mechanism. *Int. J. Environ. Res. Public Health* **2020**, *17*, 8377.
97. Ouyang, Y.; Xu, Y.; Zhao, L.; Deng, M.; Yang, P.; Peng, G.; Ke, G. Preparation of ZnNiAl-LDHs microspheres and their adsorption behavior and mechanism on U(VI). *Sci. Rep.* **2021**, *11*, 21625. [CrossRef]
98. Nachaithong, T.; Moontragoon, P.; Chanleke, N.; Thongbai, P. Fe^{3+}/Nb^{5+} Co-doped rutile–TiO_2 nanocrystalline powders prepared by a combustion process: Preparation and characterization and their giant dielectric response. *RSC Adv.* **2020**, *10*, 24784–24794. [CrossRef]

99. Zhang, S.; Yang, N.; Zhuang, X.; Ren, L.; Natarajan, V.; Cui, Z.; Si, H.; Xin, X.; Ni, S.; Zhan, J. Montmorillonite immobilized Fe/Ni bimetallic prepared by dry in-situ hydrogen reduction for the degradation of 4-Chlorophenlo. *Sci. Rep.* **2019**, *9*, 13388. [CrossRef]
100. Zhang, G.; Fan, F.; Li, X.; Qi, J.; Chen, Y. Superior adsorption of thallium(I) on titanium peroxide: Performance and mechanism. *Chem. Eng. J.* **2018**, *331*, 471–479. [CrossRef]
101. Li, H.; Li, X.; Chen, Y.; Long, J.; Zhang, G.; Xiao, T.; Zhang, P.; Li, C.; Zhuang, L.; Huang, W. Removal and recovery of thallium from aqueous solutions via a magnetite-mediated reversible adsorption-desorption process. *J. Clean. Prod.* **2018**, *199*, 705–715. [CrossRef]